Article

The Design of a Low-Loss, Fast-Response, Metal Thermo-Optic Phase Shifter Based on Coupled-Mode Theory

Weiyu Tong, Yanxian Wei, Hailong Zhou, Jianji Dong * and Xinliang Zhang

Wuhan National Laboratory for Optoelectronics, School of Optical and Electronic Information, Huazhong University of Science and Technology, Wuhan 430074, China; tongweiyu98@hust.edu.cn (W.T.); d201880716@hust.edu.cn (Y.W.); hailongzhou@hust.edu.cn (H.Z.); xlzhang@mail.hust.edu.cn (X.Z.)
***** Correspondence: jjdong@hust.edu.cn

Abstract: A thermo-optic phase shifter is of great importance in silicon photonics. However, it is difficult to simultaneously achieve a good performance in insertion loss and in response speed by using traditional thermal tuning through a metallic heater. In this paper, based on coupled-mode theory, we propose a method to place high-loss materials close to the optical waveguide while maintaining the low loss of the optical device, which ensures the low insertion loss (~0.78 dB) of the phase shifter. Additionally, thanks to the very short distance between the rib waveguide and the chromium (Cr) heater, the phase shifter exhibits a high response speed (1.15 μs in rise time and 2.18 μs in decay time) with a measured bandwidth (BW) of 186 kHz. Moreover, we further optimize the structure of phase shifters, leading to the reduction of π-shift power consumption from 25.1 mW to 13.6 mW. Our proposed phase shifters have great potential in large-scale silicon photonic integrated circuits.

Keywords: silicon photonics; phase shifter; coupled-mode theory

1. Introduction

With its low loss, high speed, large bandwidth, and high integration, silicon photonics provides new possibilities for faster, more flexible, and more effective information processing in the information era. An optical phase shifter is an indispensable component of the silicon photonics platform, since many emerging applications require the integration of a large number of optical phase shifters, such as integrated photonic quantum [1–3], optical phased array [4–6], optical neural networks [7–9], reconfigurable signal processors [10,11], arbitrary waveform generation [12,13], and so on.

Due to the high thermal conductivity (142 Wm^{-1}K^{-1} [14]) and the thermo-optic coefficient (1.84 $\times$ 10^{-4} K^{-1} [15]) of silicon, thermal tuning is widely used in optical phase shifters, and it can be easily achieved by heating the waveguide with metallic microheaters. However, to avoid optical loss, metallic heaters are usually placed far away from the waveguide (usually around 2~3 μm) in conventional designs, which could lead to a low response speed and high power consumption because of the long heat conduction distance. Although, doped silicon [16,17] and two-dimensional materials [18,19] are proposed to replace metallic heaters for fast response, the fabrication processes become relatively more complicated in these cases. Especially, a two-dimensional material-based microheater requires complex fabrication and transfer processes, which are not compatible with complementary metal oxide semiconductor (CMOS) technology. Therefore, metallic heaters are still widely used in large-scale silicon photonic integrated circuits, and how to simultaneously realize a low insertion loss and a fast response speed for the phase shifters using metallic heaters has become an urgent problem to be addressed.

In this paper, we propose and experimentally demonstrate a metal phase shifter that has both a low insertion loss and a fast response. In the phase shifter, chromium (Cr)

heater is deposited at a very short distance on the side pad of the rib waveguide for rapid heating. The design method based on the coupled-mode theory ensures the low mode loss of the phase shifter, which is experimentally measured to be 0.78 dB. The modulation performance of the phase shifter was measured through the Mach–Zehnder interferometer (MZI) structure, and the fastest response time was 1.15 µs in rise time and 2.18 µs in decay time, with a measured bandwidth (BW) of 186 kHz. In addition, we designed an improved structure of the phase shifter, reducing the π-shift power consumption (P_π) from 25.1 mW to 13.6 mW, while maintaining a high response speed.

2. Methods

Considering a system composed of two coupled rib waveguides with different losses, based on coupled-mode theory, the equations of motion for the amplitudes a_1 and a_2 in these two rib waveguides can be written as [20]:

$$i\frac{d}{dz}\begin{pmatrix} a_1 \\ a_2 \end{pmatrix} = \begin{pmatrix} \beta_1 - i\gamma_1 & \kappa \\ \kappa & \beta_2 - i\gamma_2 \end{pmatrix}\begin{pmatrix} a_1 \\ a_2 \end{pmatrix} \tag{1}$$

where β_1 and β_2 are the propagation constants of the two waveguides, γ_1 and γ_2 are the corresponding loss factors, κ is the coupling strength, and z is the propagation distance. The eigenvalue of this system can be given by:

$$\lambda_\pm = \beta - i\gamma \pm \sqrt{\kappa^2 + (d\beta - id\gamma)^2} \tag{2}$$

where $\beta = (\beta_1 + \beta_2)/2$, $\gamma = (\gamma_1 + \gamma_2)/2$, $d\beta = (\beta_1 - \beta_2)/2$, and $d\gamma = (\gamma_1 - \gamma_2)/2$. The absolute value of the imaginary part of the eigenvalue $\lambda_\pm$ (i.e., Im($\lambda_\pm$)) is proportional to the loss of the corresponding eigenmode. By normalizing Equation (2) with κ, we can reduce the number of variables and simplify the theoretical analysis that follows. Meanwhile, with the assumption of $\gamma_1 = 0$ (lossless waveguide, LWG) and $\gamma_2 > 0$ (high-loss waveguide, HWG), we can finally obtain $\lambda_\pm/\kappa$ as a function of $d\beta/\kappa$ and γ_2/κ:

$$\frac{\lambda_\pm}{\kappa} = \frac{\beta}{\kappa} - i\frac{\gamma_2}{2\kappa} \pm \sqrt{1 + \left(\frac{d\beta}{\kappa} + i\frac{\gamma_2}{2\kappa}\right)^2} \tag{3}$$

Figure 1a presents the calculated imaginary part of $\lambda_\pm/\kappa$ (i.e., Im($\lambda_\pm/\kappa$)) as a function of γ_2/κ when $|d\beta/\kappa|$ is a constant. It can be seen that with the increasing of γ_2/κ, the loss of the eigenmode corresponding to eigenvalue λ_- (mode 2) increases rapidly, and only the eigenmode corresponding to eigenvalue λ_+ (mode 1) can still transmit with a low loss, which ultimately manifests as light being confined in a lossless waveguide. Figure 1b intuitively shows the variation of the eigenmode distribution and the propagation field in the coupled system with the increase of γ_2/κ. We can conclude that when γ_2/κ is large, mode 2 will decay rapidly, the two eigenmodes will decouple, and the light will be confined in the lossless waveguide.

Specific to mode 1, Figure 1c shows calculated Im(λ_+/κ) as a function of γ_2/κ at different $|d\beta/\kappa|$. For the system with a particular coupling strength κ, the mode loss first grows with the increasing of γ_2, until it reaches the maximum value. After that, the mode loss will counterintuitively decrease with the increase of γ_2. Furthermore, we can see from the curves corresponding to different $|d\beta/\kappa|$ that the mode loss will monotonically decrease with the increase of $|d\beta/\kappa|$. Therefore, there are two ways to reduce the insertion loss when the coupling strength κ remains constant. One is by increasing the $|d\beta|$, which is affected by the real refractive index difference between the two waveguides, another is by reducing or sufficiently increasing the inherent loss (i.e., the imaginary part of the refractive index) of the high-loss waveguide. Therefore, by treating the metallic heater as a high-loss waveguide, when the heater is very close to the waveguide, the phase shifter can achieve a low loss by choosing a metal with a suitable complex index of refraction, instead of simply placing the metallic heater far enough away to reduce waveguide-metal coupling

(i.e., decrease κ), as in previous schemes. The dotted oval box annotation in Figure 1b shows the difference between our scheme and previous schemes. We achieve a low loss by balancing the three parameters of $d\beta$, γ_2 and κ, while the previous schemes ignore the metal type and simply make κ close to 0 through the long distance between the waveguide and the heater to achieve a low loss.
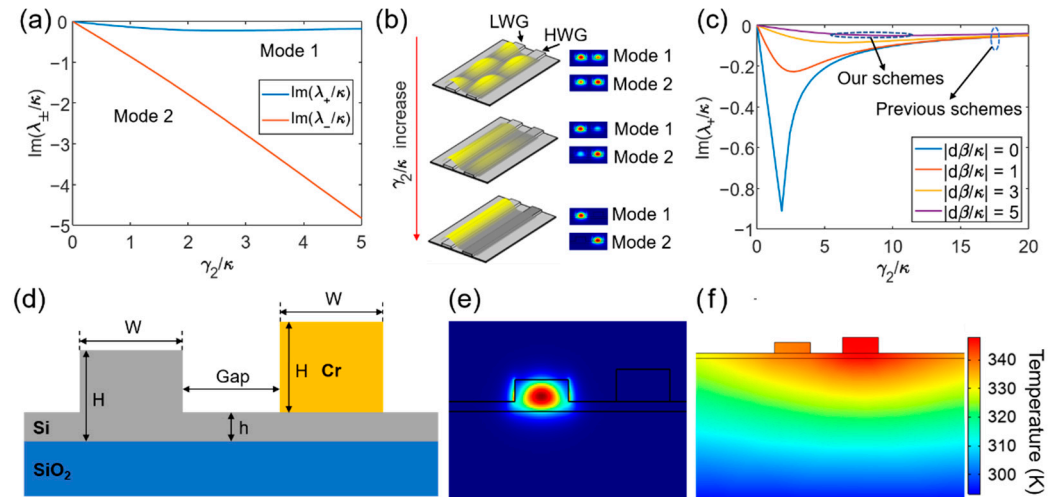
Figure 1. (**a**) The imaginary parts of $\lambda_\pm/\kappa$ vary with γ_2/κ when $|d\beta/\kappa| = 1$. (**b**) Schematic diagrams of the eigenmode distribution and the propagation field as γ_2/κ increases. (**c**) The imaginary part of λ_+/κ vary with γ_2/κ at different $|d\beta/\kappa|$. (**d**) Simplified cross-sectional diagram of the phase shifter, not to scale. W = 500 nm, H = 220 nm, h = 70 nm, Gap = 350, 450, and 550 nm. (**e**) Simulated optical E field distribution for the fundamental mode at a wavelength of 1550 nm (Gap = 450 nm). (**f**) Simulated temperature distribution at P_π = 25.1 mW (Gap = 450 nm).

Based on the above principles, we designed a phase shifter using a metallic heater on a silicon-on-insulator (SOI) substrate, and Figure 1d shows its cross-sectional view. It comprises a rib waveguide and a Cr strip placed very close to the side of the rib region. The ridge waveguide was fabricated by etching 150 nm deep on an SOI substrate with a top silicon thickness of 220 nm and the width of the rib region is 500 nm, and the Cr heater was also 220 nm thick and 500 nm wide. The gap between the rib region and the Cr heater was 350, 450, and 550 nm. The longitudinal length of the phase shifter was 100 μm. Because of the short distance and the direct contact through silicon between the Cr heater and the rib region, the heat generated by the Cr heater can be quickly conducted to the rib region, so a high response speed can be expected.

With the designed parameters of W = 500 nm, H = 220 nm, h = 70 nm, and Gap = 450 nm in Figure 1d, the optical E field distribution of the designed phase shifter at 1550 nm is shown in Figure 1e. The simulation result was calculated by the finite-difference-time-domain (FDTD) method. The optical field is well confined in the rib region with an insertion loss of 0.48 dB. Figure 1f shows the temperature distribution in a cross section of the phase shifter simulated by COMSOL Multiphysics. The boundary conditions with a constant ambient temperature of 293 K at the boundaries of the silicon substrate and a fixed convection of 10 W/m²·K at the boundaries of the open-air region were set; 25.1 mW (P_π measured in the following experiments) was applied on the Cr heater, and the temperature at the center of the rib waveguide was heated up to 339 K.

3. Results

We first measured the insertion loss of the phase shifter. Figure 2a shows the measured transmission spectra of the phase shifters with different gaps and the reference rib waveguide without the Cr heater. The experimental configuration is presented in Figure 3a. An amplified spontaneous emission (ASE, OS8143) optical source was used to generate

a C-band broadband signal. An optical isolator was used to ensure the unidirectional transmission of light, and a polarization controller (PC) was used to ensure proper input polarization to the chip. After passing through the phase shifter, the output light was characterized by optical spectrum analyzer (OSA, Yokokawa, AQ6319) for the spectrum. By comparing the spectra of phase shifters with reference spectrum, we can calculate that the insertion losses introduced by the Cr heaters was 2.40 dB, 0.78 dB, and 0.15 dB at different gaps. Figure 2b shows a comparison of the simulated and the experimental results of insertion losses. The scattering of light on the rough surface of the fabricated waveguides and the fabrication errors, such as the deposition residue on the edge of the Cr heater (shown in SEM images below), cause the actual insertion losses to increase compared to the simulated results.
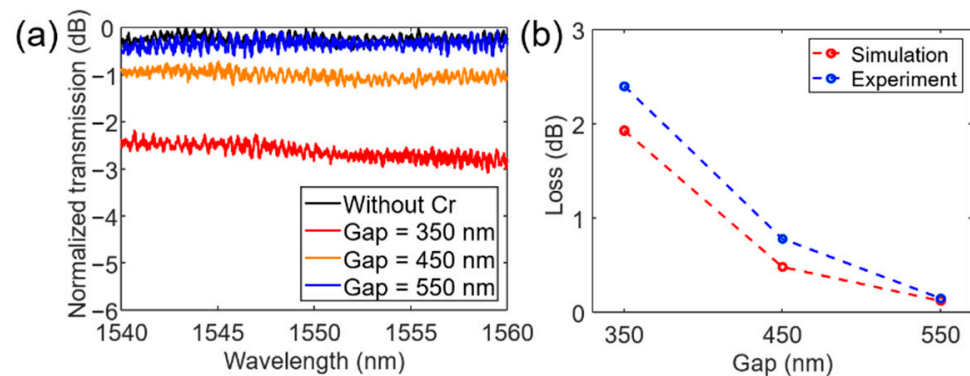
Figure 2. (**a**) Measured transmission spectra of reference rib waveguide and phase shifters with different gaps. (**b**) Measured (blue circle) and simulated (red circle) insertion losses for different gaps.
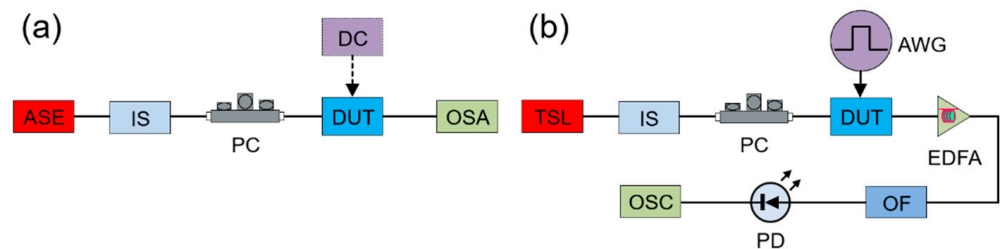

Figure 3. (**a**,**b**) Block diagrams of the experimental setups for the characterization of the phase shifters. ASE, amplified spontaneous emission optical source; IS, optical isolator; PC, polarization controller; DUT, device under test; OSA, optical spectrum analyzer; DC, direct current source; TSL, tunable laser source; AWG, arbitrary waveform generator; EDFA, erbium-doped optical fiber amplifier; OF, optical filter; PD, photodiode; OSC, Oscilloscope.

　　To verify the modulation performance of the phase shifter, we placed the designed phase shifter on one arm of MZI structure. Figure 3a with the direct current (DC) source presents the experimental setup used to measure the spectra of the MZI structure at different driving powers. Figure 3b presents the experimental setup used to measure the dynamic response of the MZI structure. The wavelength of tunable laser source (TLS, Alnair Labs, TLG-200) is set at an interference dip around 1550 nm. An Erbium-doped fiber amplifier (EDFA) is incorporated to amplify the output signal, and an optical filter (OF) after EDFA mitigates the amplified spontaneous emission noise. The optical signal modulated by the arbitrary waveform generator (AWG, RIGOL, DG4202) is converted into an electrical signal by a photodiode (PD, Discovery, DSC40S), and it is displayed on the oscilloscope (OSC, RIGOL, DG4022).

　　Figure 4a shows the microscope image of the MZI structure we fabricated. The rib waveguide and the Cr heater are fabricated in the two MZI arms to balance the optical loss, both 100 μm in length. The corresponding fabrication areas are marked with red

dashed boxes in Figure 4a. Outside the box are ordinary strip waveguides with a cross section of 500 nm × 220 nm. The pad of the rib waveguide is connected to the ordinary strip waveguides through a 20 µm long taper with a width of 0.5 µm and 6.5 µm at two ends, respectively. Figure 4b shows the scanning electron microscope (SEM) image of the phase shifter.
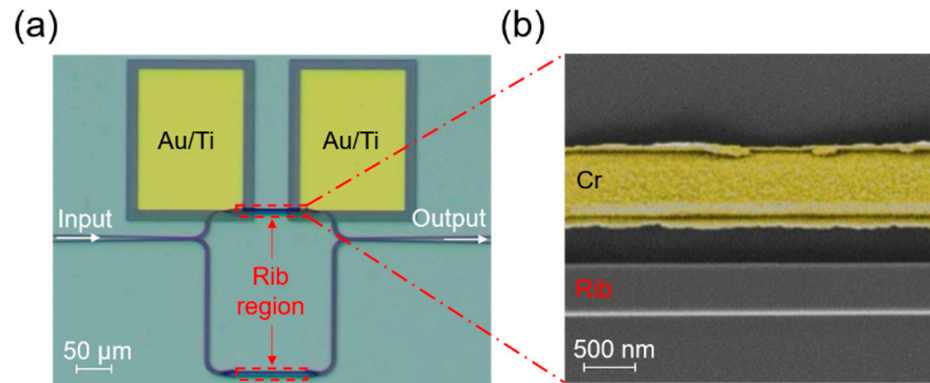
Figure 4. (**a**) Microscope image of the MZI structure. (**b**) The zoom in SEM image of the phase shifter. Cr heater is false colored.

Figure 5a–c present the corresponding measured results when the gap between the rib waveguide and the Cr heater is 450 nm. Figure 5a presents the transmission spectra when different driving power is applied to the Cr heater. Since we place the phase shifter on the short arm of the MZI structure, the transmission spectra blue shifts as the driving power increases. Figure 5b shows that the shift of the transmission spectra with increasing driving power is linear, and the tuning efficiency is 0.0347 nm/mW. The red dots, respectively, correspond to the different driving powers and corresponding resonance shifts in Figure 5a, and the one pointed by the black arrows indicate that the π-shift power consumption is 25.1 mW.
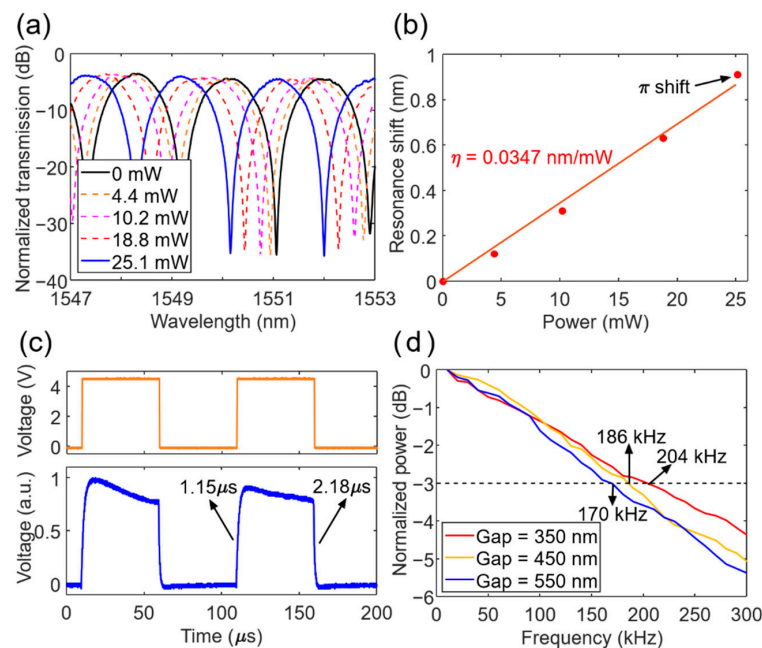
Figure 5. (**a**) Transmission spectra of the MZI for different heating powers (Gap = 450 nm). (**b**) Resonance shifts for the interference dips at 1551.06 nm for different heating powers (Gap = 450 nm). (**c**) Driving signal (orange line) and corresponding response signal (blue line) (Gap = 450 nm). (**d**) Measured 3-dB bandwidth for different gaps.

A 10 kHz square-wave signal (shown as the orange line in Figure 5c) generated by the AWG is used to drive the Cr heater to measure the dynamic response of the phase shifter. The amplitude of the square-wave signal is 4.4 V, which is the half-wave voltage of the phase shifter. The blue line in Figure 5c shows the corresponding normalized output signal. Its rise time (from 10–90%) and its decay time (from 90–10%) are 1.15 µs and 2.18 µs, respectively. Figure 5d shows the measured 3-dB bandwidth of the phase shifter for different gaps.

To reduce the power consumption of the phase shifter, we designed the second structure (type II) shown in Figure 6a, and Figure 6b shows its SEM image. Type II is essentially to additionally perform full etching on both sides of the rib waveguide in the aforementioned structure (type I). Through the air grooves on both sides to block the heat conduction in the silicon, the heat generated by the Cr heater can be better confined around the rib region, thereby reducing power consumption.
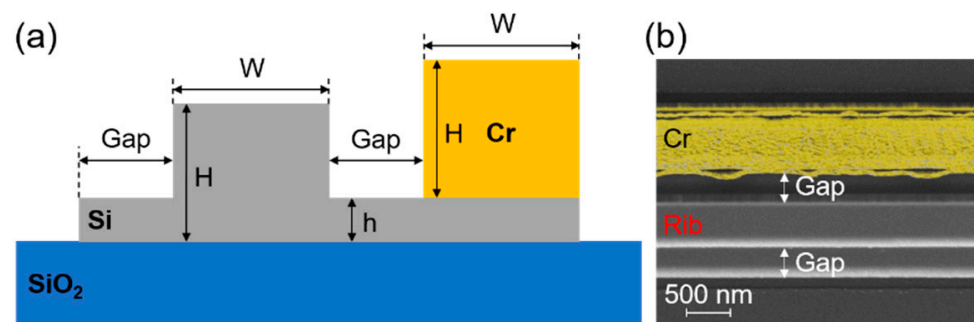
Figure 6. (**a**) Simplified cross-sectional diagram of the phase shifter (type II), not to scale. The parameters are the same as the phase shifter (type I) shown in Figure 1c. (**b**) SEM image of the phase shifter (type II). Cr heater is false colored.

Figure 7a shows that the tuning efficiency of the type II phase shifter with Gap = 450 nm is 0.0615 nm/mW, which is significantly improved compared to the type I phase shifter. The red dot pointed by the black arrow indicates that the π-shift power consumption is 13.6 mW. Figure 7b shows the measured 3-dB bandwidth of the type II phase shifter for different gaps. Since the fabrication failed when Gap = 350 nm, the corresponding performances are not presented.

Figure 7c shows the measured response time of the two different phase shifters for different gaps. The response time in the figure is obtained from the average of the rise time and the decay time. The circles and the squares represent the average of the experimental results of different devices with the same designed parameters on the chip. The corresponding average values are 1.71 µs, 1.87 µs, and 2.08 µs for type I phase shifters and 1.92 µs and 1.90 µs for type II phase shifters. The length of the vertical line represents the value of the corresponding sample standard deviation. Although the phase shifters on these MZI structures are designed with the same gap (Gap = 350, 450, or 550 nm), there are different fabrication errors in practice, so the average value of type II phase shifters measured at Gap = 550 nm is slightly smaller than that measured at Gap = 450 nm. Figure 7d shows the comparison of the π-shift power consumption of two different phase shifters. The corresponding average values are 25.2 mW, 27.6 mW, and 28.1 mW for type I phase shifters and 14.6 mW and 16.2 mW for type II phase shifters. We can see that the optimized structure can reduce the power consumption of the phase shifters by approximately 10 mW for different gaps, without significantly degrading their thermal tuning speed.
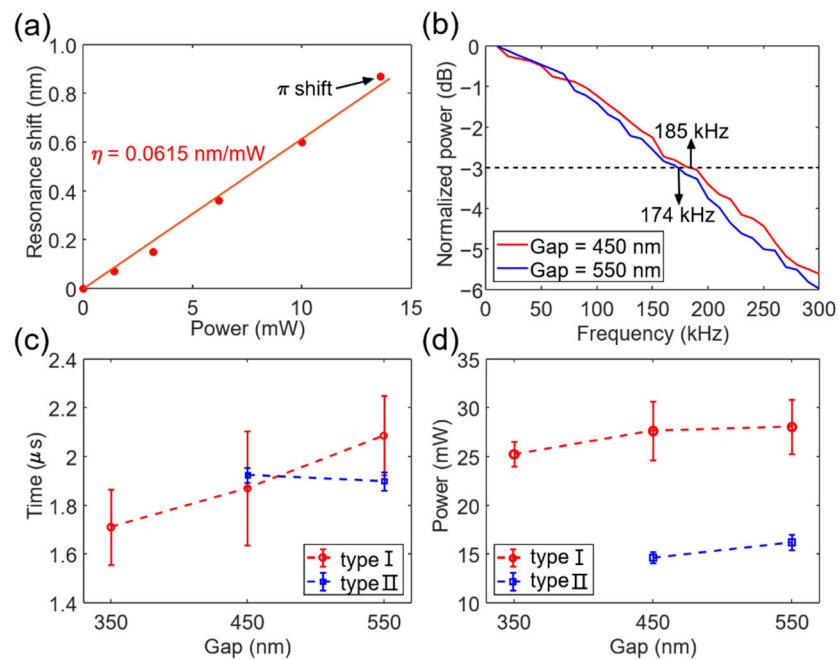
Figure 7. (**a**) Resonance shifts for the interference dips at 1549.75 nm for different heating powers (Gap = 450 nm). (**b**) Measured 3-dB bandwidth for different gaps. (**c**) Measured response time (the average of rise time and decay time) for different gaps. (**d**) Measured power consumption for different gaps.

4. Discussion

Table 1 shows a comparison of the proposed schemes with the state-of-art phase shifters using metallic heaters demonstrated on a silicon platform in recent years [21–24]. The τ is the thermal time constant. In references where τ is not reported, the τ in Table 1 is calculated based on the single-pole approximation ($\tau = 0.35/\text{BW}$).

Table 1. Comparison of experimental results with phase shifters using metallic heaters.

Scheme	Loss [dB]	BW (τ) [kHz (μs)]	P_π [mW]	Ref
Optimum TiN heater	0.4	62 (5.6)	21.4	[21]
Multi-pass structure with W heater	1.2	54 (6.5)	1.7	[22]
Silicon spiral waveguide with Ti heater	0.9	39 (9)	3.0	[23]
Silicon-rich silicon nitride with Ni:Cr heater	1.2	15 (23)	8.0	[24]
Our scheme (type I)	0.78	186 (1.87)	25.1	\
Our scheme (type II)	0.96	185 (1.92)	13.6	\

Compared to other schemes, our designed phase shifter achieves both a low insertion loss and a much faster response speed based on a simple structure and conventional material. In this work, a thermo-optical phase shifter using Cr to heat the rib waveguide at a very short distance is proposed and experimentally demonstrated. It has a low insertion loss (0.78 dB) and a fast response (1.15 μs in rise time and 2.18 μs in decay time) at the same time, and its π-shift power consumption is reduced from 25.1 mW to 13.6 mW by optimizing the structure. In addition, the phase shifter is fabricated only by the two standard silicon photonic fabrication processes of rib waveguide etching and heating metal deposition, without the need for silicon air trenches or undercut process. Because of its excellent performance and its simple fabrication, we believe that the proposed phase shifters have great potential in large-scale silicon photonics integrated circuits.

Institutional Review Board Statement: Not applicable.

Informed Consent Statement: Not applicable.

Data Availability Statement: The data that support the findings of this study are available from the corresponding author upon reasonable request.

Conflicts of Interest: The authors declare no conflict of interest.

References

1. Wang, J.W.; Paesani, S.; Ding, Y.H.; Santagati, R.; Skrzypczyk, P.; Salavrakos, A.; Tura, J.; Augusiak, R.; Mancinska, L.; Bacco, D.; et al. Multidimensional quantum entanglement with large-scale integrated optics. *Science* **2018**, *360*, 285–291. [CrossRef] [PubMed]
2. Chen, X.; Deng, Y.; Liu, S.; Pramanik, T.; Mao, J.; Bao, J.; Zhai, C.; Dai, T.; Yuan, H.; Guo, J.; et al. A generalized multipath delayed-choice experiment on a large-scale quantum nanophotonic chip. *Nat. Commun.* **2021**, *12*, 2712. [CrossRef]
3. Zheng, X.; Zhang, P.; Ge, R.; Lu, L.; He, G.; Chen, Q.; Qu, F.; Zhang, L.; Cai, X.; Lu, Y.; et al. Heterogeneously integrated, superconducting silicon-photonic platform for measurement-device-independent quantum key distribution. *Adv. Photonics* **2021**, *3*, 055002. [CrossRef]
4. Sun, J.; Timurdogan, E.; Yaacobi, A.; Hosseini, E.S.; Watts, M.R. Large-scale nanophotonic phased array. *Nature* **2013**, *493*, 195–199. [CrossRef] [PubMed]
5. Hutchison, D.N.; Sun, J.; Doylend, J.K.; Kumar, R.; Heck, J.; Kim, W.; Phare, C.T.; Feshali, A.; Rong, H. High-resolution aliasing-free optical beam steering. *Optica* **2016**, *3*, 887–890. [CrossRef]
6. Poulton, C.V.; Yaacobi, A.; Cole, D.B.; Byrd, M.J.; Raval, M.; Vermeulen, D.; Watts, M.R. Coherent solid-state LIDAR with silicon photonic optical phased arrays. *Opt. Lett.* **2017**, *42*, 4091–4094. [CrossRef]
7. Shen, Y.; Harris, N.C.; Skirlo, S.; Prabhu, M.; Baehr-Jones, T.; Hochberg, M.; Sun, X.; Zhao, S.; Larochelle, H.; Englund, D.; et al. Deep learning with coherent nanophotonic circuits. *Nat. Photonics* **2017**, *11*, 441–446. [CrossRef]
8. Harris, N.C.; Carolan, J.; Bunandar, D.; Prabhu, M.; Hochberg, M.; Baehr-Jones, T.; Fanto, M.L.; Smith, A.M.; Tison, C.C.; Alsing, P.M.; et al. Linear programmable nanophotonic processors. *Optica* **2018**, *5*, 1623–1631. [CrossRef]
9. Bogaerts, W.; Pérez, D.; Capmany, J.; Miller, D.A.B.; Poon, J.; Englund, D.; Morichetti, F.; Melloni, A. Programmable photonic circuits. *Nature* **2020**, *586*, 207–216. [CrossRef]
10. Zhuang, L.; Roeloffzen, C.G.H.; Hoekman, M.; Boller, K.-J.; Lowery, A.J. Programmable photonic signal processor chip for radiofrequency applications. *Optica* **2015**, *2*, 854–859. [CrossRef]
11. Pérez, D.; Gasulla, I.; Crudgington, L.; Thomson, D.J.; Khokhar, A.Z.; Li, K.; Cao, W.; Mashanovich, G.Z.; Capmany, J. Multipurpose silicon photonics signal processor core. *Nat. Commun.* **2017**, *8*, 636. [CrossRef] [PubMed]
12. Khan, M.H.; Shen, H.; Xuan, Y.; Zhao, L.; Xiao, S.; Leaird, D.E.; Weiner, A.M.; Qi, M. Ultrabroad-bandwidth arbitrary radiofrequency waveform generation with a silicon photonic chip-based spectral shaper. *Nat. Photonics* **2010**, *4*, 117–122. [CrossRef]
13. Liao, S.; Ding, Y.; Dong, J.; Yang, T.; Chen, X.; Gao, D.; Zhang, X. Arbitrary waveform generator and differentiator employing an integrated optical pulse shaper. *Opt. Express* **2015**, *23*, 12161–12173. [CrossRef]
14. Shanks, H.R.; Maycock, P.D.; Sidles, P.H.; Danielson, G.C. Thermal Conductivity of Silicon from 300 to 1400°K. *Phys. Rev.* **1963**, *130*, 1743–1748. [CrossRef]
15. Espinola, R.L.; Tsai, M.C.; Yardley, J.T.; Osgood, R.M. Fast and low-power thermooptic switch on thin silicon-on-insulator. *IEEE Photonics Technol. Lett.* **2003**, *15*, 1366–1368. [CrossRef]
16. Mendez-Astudillo, M.; Okamoto, M.; Ito, Y.; Kita, T. Compact thermo-optic MZI switch in silicon-on-insulator using direct carrier injection. *Opt. Express* **2019**, *27*, 899–906. [CrossRef]
17. Zhong, C.; Ma, H.; Sun, C.; Wei, M.; Ye, Y.; Tang, B.; Zhang, P.; Liu, R.; Li, J.; Li, L.; et al. Fast thermo-optical modulators with doped-silicon heaters operating at 2 mum. *Opt. Express* **2021**, *29*, 23508–23516. [CrossRef] [PubMed]
18. Yan, S.; Zhu, X.; Frandsen, L.H.; Xiao, S.; Mortensen, N.A.; Dong, J.; Ding, Y. Slow-light-enhanced energy efficiency for graphene microheaters on silicon photonic crystal waveguides. *Nat. Commun.* **2017**, *8*, 14411. [CrossRef] [PubMed]
19. Cheng, Z.; Cao, R.; Guo, J.; Yao, Y.; Wei, K.; Gao, S.; Wang, Y.; Dong, J.; Zhang, H. Phosphorene-assisted silicon photonic modulator with fast response time. *Nanophotonics* **2020**, *9*, 1973–1979. [CrossRef]
20. Milburn, T.J.; Doppler, J.; Holmes, C.A.; Portolan, S.; Rotter, S.; Rabl, P. General description of quasiadiabatic dynamical phenomena near exceptional points. *Phys. Rev. A* **2015**, *92*, 052124. [CrossRef]

21. Jacques, M.; Samani, A.; El-Fiky, E.; Patel, D.; Xing, Z.; Plant, D.V. Optimization of thermo-optic phase-shifter design and mitigation of thermal crosstalk on the SOI platform. *Opt. Express* **2019**, *27*, 10456–10471. [CrossRef] [PubMed]
22. Miller, S.A.; Chang, Y.-C.; Phare, C.T.; Shin, M.C.; Zadka, M.; Roberts, S.P.; Stern, B.; Ji, X.; Mohanty, A.; Jimenez Gordillo, O.A.; et al. Large-scale optical phased array using a low-power multi-pass silicon photonic platform. *Optica* **2020**, *7*, 3–6. [CrossRef]
23. Qiu, H.; Liu, Y.; Luan, C.; Kong, D.; Guan, X.; Ding, Y.; Hu, H. Energy-efficient thermo-optic silicon phase shifter with well-balanced overall performance. *Opt. Lett.* **2020**, *45*, 4806–4809. [CrossRef] [PubMed]
24. Nejadriahi, H.; Pappert, S.; Fainman, Y.; Yu, P. Efficient and compact thermo-optic phase shifter in silicon-rich silicon nitride. *Opt. Lett.* **2021**, *46*, 4646–4649. [CrossRef] [PubMed]